

Heterogeneity, growing lengthscales, and universality in the dynamics of kinetically constrained lattice gases in two dimensions

Albert C. Pan,¹ Juan P. Garrahan,² and David Chandler¹

¹*Department of Chemistry, University of California, Berkeley, CA 94720-1460*

²*School of Physics and Astronomy, University of Nottingham, Nottingham, NG7 2RD, UK*

(Dated: May 23, 2019)

We study dynamical heterogeneity and growing dynamical lengthscales in two kinetically constrained models, namely, the one- and two-vacancy assisted triangular lattice gases. One of the models is a strong glassformer and the other is a fragile glassformer. Both exhibit heterogeneous dynamics with broadly distributed timescales as seen in the distribution of persistence times. We show that the Stokes-Einstein relation is violated, to a greater degree in the fragile glassformer, and show how this violation is related to dynamic heterogeneity. Finally, we extract dynamical lengthscales from structure factors of mobile particles and show, quantitatively, the growth of this lengthscale as density increases. Our results indicate that the one-vacancy assisted lattice gas is in the same universality class as the one-spin facilitated Fredrickson-Andersen model, while the two-vacancy assisted model is in a different universality class. Our findings support the idea that the dynamics of supercooled liquids can be understood from the existence of a zero temperature dynamic critical point.

PACS numbers: 05.20.Jj, 05.70.Jk, 64.70.Pf

I. INTRODUCTION

The dramatic dynamical slowdown accompanying the formation of a glass is a remarkable phenomenon [1, 2, 3]. One explanation for the underlying microscopic cause of this slowdown relies on the presence of local steric constraints on the movement of particles which make themselves felt to an increasing degree as the temperature is lowered (or the concentration of particles is increased). Kinetically constrained lattice gas models [4, 5, 6] are simple caricatures of glassformers which employ local steric constraints as their sole means to glassiness in the *absence* of any non-trivial static correlations between particles (for alternative thermodynamic views of the glass transition see e.g. [7, 8]). These constrained models have been extensively studied (see e.g. [4, 5, 9, 10, 11]). Our purpose here is to extend these studies to focus on the idea of dynamical heterogeneity [12, 13, 14] as a manifestation of excitation lines in space-time and to identify scaling and universality classes in the dynamics of these models [15, 16, 17, 18, 19].

The paper is organized as follows. Section II describes the two models we use as well as details of the computer simulations used to study them. Section III looks at heterogeneous dynamics in our models via the distribution of persistence times. Section IV presents the scaling of the structural relaxation time and diffusion constant, the implications of which lead to a discussion of the breakdown of the Stokes-Einstein relation in section V. Section VI discusses the emergence of a dynamical lengthscale and gives a quantitative characterization of this length by analyzing structure factors of mobile particles. Finally, we end with a discussion of our results in Section VII.

II. MODELS AND COMPUTATIONAL DETAILS

We present results for two kinetically constrained triangular lattice gas (TLG) models introduced by Jäckle and Krönig [5]. These two-dimensional models are variants of lattice models proposed by Kob and Andersen [4]. Each site of the triangular lattice has six nearest neighbor sites and can hold at most one particle. A particle at site \mathbf{i} is allowed to move to a nearest neighbor site, \mathbf{i}' , if (i) \mathbf{i}' is not occupied and (ii) the two mutual nearest neighbor sites of \mathbf{i} and \mathbf{i}' are also empty. These rules coincide with a physical interpretation of steric constraints on the movement of hard core particles in a dense fluid [5]. We call the model with these rules the (2)-TLG because both mutual nearest neighbors need to be empty in order to facilitate movement. We also present results for the (1)-TLG where the constraints are more relaxed: movement is allowed as long as either of the mutual nearest neighbors is empty. As with other kinetically constrained lattice gas models, the TLG has no static interactions between particles other than those that prohibit multiple occupancy of a single lattice site. Therefore, initial configurations can be generated by random occupation of empty lattice sites by particles until the desired density is reached.

In the computer simulations, we investigated particle densities, ρ , between 0.01 and 0.80 for the (2)-TLG and between 0.01 and 0.996 for the (1)-TLG. The density $\rho = 1$ corresponds to the completely full lattice in both cases. For the (2)-TLG, we used a lattice with edge length $L = 128$ for all densities. There exists the possibility in the (2)-TLG of initial configurations containing an unmoveable structure which percolates throughout the system called a backbone [4, 5]. Since the dynamics obey detailed balance, these backbones could never be destroyed in the course of the simulation. For the densities studied

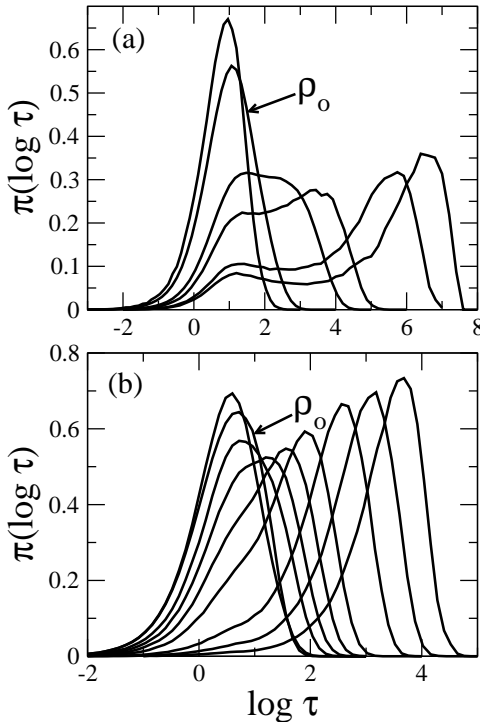


FIG. 1: Distribution of local persistence times for (a) the (2)-TLG model (from left to right) $\rho = 0.40, 0.50, 0.65, 0.70, 0.77$ and 0.79 ; and (b) the (1)-TLG model (from left to right) $\rho = 0.20, 0.60, 0.70, 0.75, 0.80, 0.85, 0.92, 0.95$ and 0.97 . The abscissae are given on a scale of logarithm base 10.

here, however, $L = 128$ is sufficiently large such that the probability of having such a configuration is vanishingly small (see [5]). For the (1)-TLG, we used $L = 128$ for densities up to and including $\rho = 0.98$. For $\rho = 0.99$ and 0.993 , we used $L = 256$ and for $\rho = 0.995$ and 0.996 , we used $L = 512$. A pair of vacancies in the (1)-TLG can always diffuse freely [5] so this version of the TLG does not suffer from the problem of backbones in the same way as the (2)-TLG. At higher densities, however, one still needs to ensure that there are a sufficient number of potentially mobile particles in the system such that the typical dynamics of the model are observed. For the (1)-TLG, the number of potentially mobile particles at higher densities is approximately equivalent to the number of vacancy pairs and therefore can be estimated as $(1 - \rho)^2 L^2$. The system sizes at the various densities for the (1)-TLG simulations were chosen such that the number of potentially mobile particles estimated in this way was always greater than or equal to 10. For both models, periodic boundary conditions were used.

At each density, several hundred independent trajectories of lengths 10-100 times τ_α , where τ_α is the time for the self-intermediate scattering function at $\mathbf{q} = (\pi, 0)$ [20] to reach $1/e$ of its initial value (see below), were run. Trajectories were stored logarithmically for later analysis (i.e. configurations were saved after 1, 2, 4, 8, 16, 32, etc. sweeps). At each state point, between 128 and 256

independent trajectories were acquired. Time was measured in Monte Carlo sweeps. During each sweep, particles were chosen randomly and a move was attempted. For the higher density runs in both models, a continuous time algorithm was used for greater efficiency [21]. This algorithm involved making and updating a list of only those particles which have the possibility of moving and choosing from among those exclusively during every move. The total time (in units of Monte Carlo sweeps) was then updated accordingly by adding to it the inverse of the number of mobile particles available during that continuous time step. The continuous time algorithm resulted in a speed up of our simulations by as much as 1-2 orders of magnitude for the highest density runs in both the (1)-TLG and the (2)-TLG. Finally, for the distribution of site persistence times (see below), statistics were gathered over runs of very large systems ($L = 1024$ and 2048).

III. HETEROGENEOUS DYNAMICS AND THE DISTRIBUTION OF PERSISTENCE TIMES

A central phenomenon behind our perspective of glasses is dynamical heterogeneity [12, 13]. A direct measure of heterogeneous dynamics in glassy systems is the

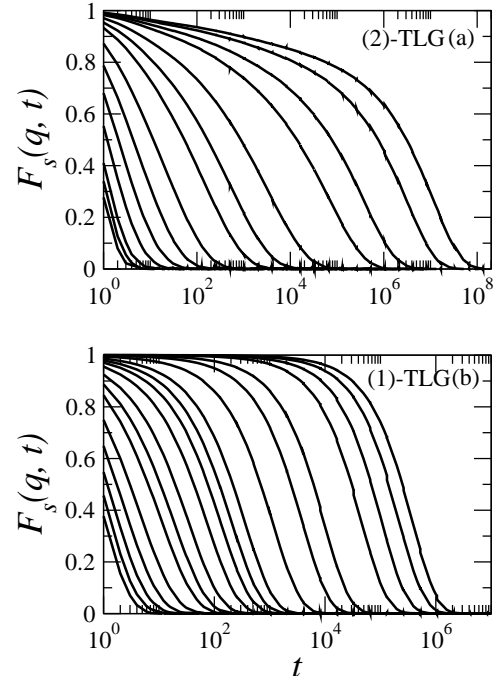


FIG. 2: Self-intermediate scattering function at wavevector $\mathbf{q} = (\pi, 0)$ for (a) the (2)-TLG (from left to right) $\rho = 0.01, 0.05, 0.10, 0.20, 0.30, 0.40, 0.50, 0.60, 0.65, 0.70, 0.75, 0.77, 0.79, 0.80$; and (b) the (1)-TLG (from left to right) $\rho = 0.20, 0.30, 0.40, 0.50, 0.60, 0.70, 0.75, 0.80, 0.85, 0.88, 0.90, 0.92, 0.95, 0.97, 0.98, 0.99, 0.993, 0.995, 0.996$. The unit of length is the lattice spacing.

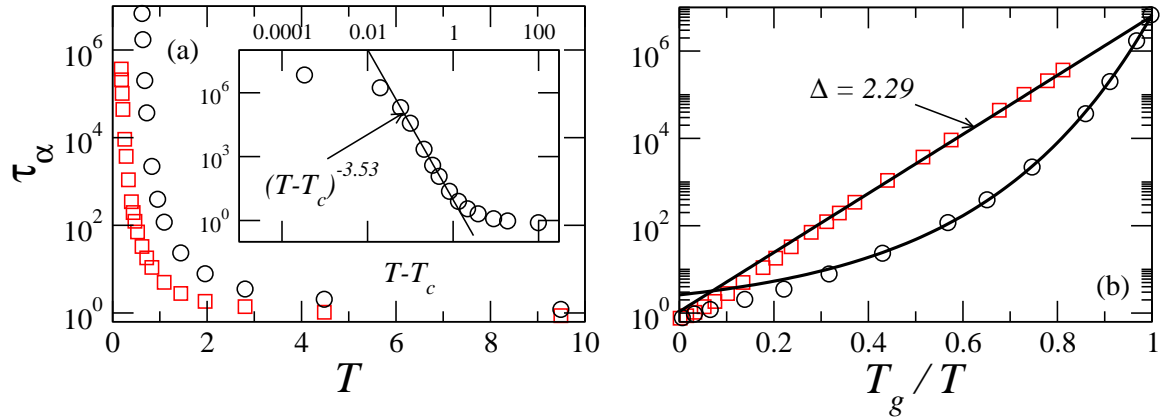


FIG. 3: (a) Structural relaxation time as a function of temperature. Circles and squares correspond to the (2)-TLG and (1)-TLG, respectively, throughout the paper. The inset shows the same data for the (2)-TLG plotted versus $T - T_c$ and a power law fit (solid line) to a portion of the data. (b) Structural relaxation as a function of scaled reciprocal temperature. Here T_g is such that $\tau_\alpha(T_g) = 10^7$. The lines are fits to the relaxation times at low temperatures. For the (1)-TLG we use the Arrhenius form $\ln \tau_\alpha \propto \Delta/T$, with $\Delta \approx 2.29$. For the (2)-TLG we use a double exponential [10], $\ln \tau_\alpha \propto \exp(a/T)$, with $a \approx 1.76$.

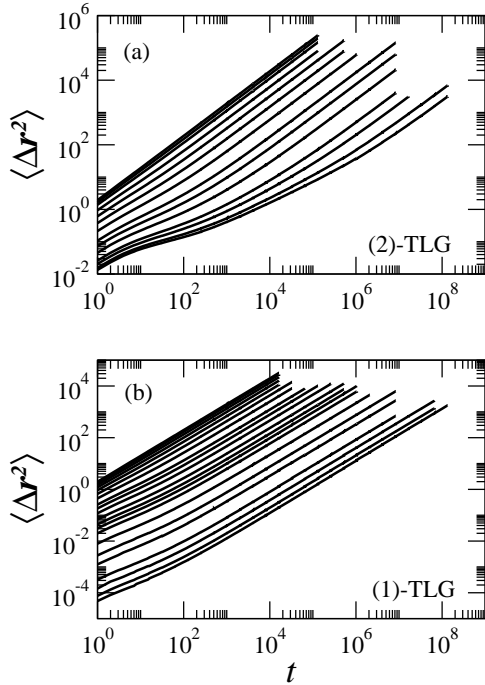


FIG. 4: The mean-squared displacement: (a) the (2)-TLG, $\rho = 0.01$ to 0.80 ; (b) the (1)-TLG, $\rho = 0.01$ to 0.996 .

idea of persistence times [16, 17]. Fig. 1(a) and Fig. 1(b) show the distribution of site persistence times, $\pi(\log \tau)$, in the (2)-TLG and (1)-TLG at various densities; that is, the distribution of times, given an initial configuration of the lattice, before the first change at a particular site occurs, either due to an empty site being filled or a filled site becoming empty. These distributions are multi-point functions because they depend not only on the state of a lattice site at the initial time and the time

when it changes, but also on all intervening points in time. As has been shown in spin-facilitated models [16], three distinct dynamical regimes are observed: (i) at low densities, there is a single peak at small relaxation times indicating homogeneous fast dynamics; (ii) at intermediate densities, two peaks develop and co-exist, one at faster times and the other at slower times, indicating heterogeneous, fluctuation dominated, dynamics; (iii) as density is increased even higher, the peak at faster times becomes suppressed relative to the peak at slower times and the dynamics again become homogeneous and slow. In region (ii), or the crossover region, the dynamics are broadly distributed over several orders of magnitude in time. Following Ref. [16], we can define, qualitatively, an onset density, ρ_o , for both models where the dynamics begin to feel the influence of dynamical heterogeneity and thereby lose their mean-field character, as well as a crossover density ρ_c where slow processes begin to dominate. For the (2)-TLG, $\rho_o = 0.50$ and (we anticipate) $\rho_c = 0.80$ and for the (1)-TLG, $\rho_o = 0.60$ and $\rho_c = 0.85$.

In the next section, we turn to two two-point functions which have been the more conventional measures of glassy dynamics: the self-intermediate scattering function and the mean-squared displacement.

IV. DYNAMICAL SLOWDOWN

A basic ingredient of a glassformer is a precipitous dynamical slowdown over a narrow range of temperatures or densities. This characteristic can already be seen qualitatively in the distribution of persistence times by looking at the movement of the mean of the distributions as ρ increases. For example, in the (2)-TLG, from $\rho = 0.70$ to $\rho = 0.77$, the mean persistence time increase 2-3 orders of magnitude. The traditional measure of this slow-

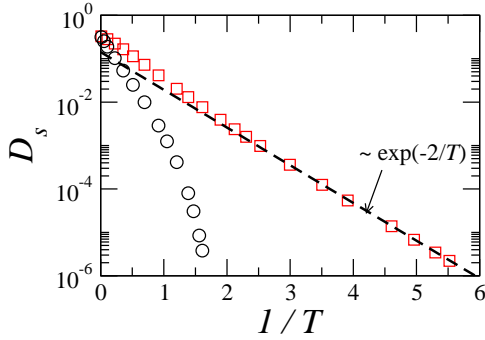


FIG. 5: Self-diffusion constant as a function of inverse temperature.

down is the self-intermediate scattering function, $F_s(q, t) = \langle e^{i\mathbf{q} \cdot (\mathbf{r}_i(t) - \mathbf{r}_i(0))} \rangle$, particularly its decay at wavevector $\mathbf{q} = (\pi, 0)$, Fig. 2(a) and Fig. 2(b). Here, $\mathbf{r}_i(t)$ denotes the position of particle i at time t . The angled brackets, $\langle \dots \rangle$, denote an average over different pairs of configurations along a trajectory separated by a given time interval. The decay of the scattering function to $1/e$ at this wavevector is typically defined to be τ_α , or the structural relaxation time, as it gives a sense of how density fluctuations relax at relatively short lengthscales.

Experiments report the scaling of viscosity versus inverse temperature [2]. Therefore, for the particular case of a kinetic lattice gas, one would like to make connections between structural relaxation time and viscosity, and density and inverse temperature. In both experiments and computer simulations [22, 23], it has been shown that the structural relaxation time scales like the viscosity. If one imagines that the concentration of vacancies, c , in the TLG models are like excitations or fluctuating regions of high energy, then it is reasonable to define a reduced temperature, T , such that $c \equiv (1 - \rho) \equiv e^{-1/T}$ or:

$$-\ln(1 - \rho) \equiv 1/T. \quad (1)$$

The structural relaxation time plotted versus T and $1/T$ is shown in Fig. 3(a) and Fig. 3(b), respectively. The inset of Fig. 3(a) shows a plot of τ_α versus $T - T_c$ for the (2)-TLG where T_c is taken to be the temperature at the crossover density, ρ_c (as defined in section III), and the black line is a power law fit to a portion of the data in the manner of mode coupling theory (MCT) [24]. In MCT, T_c is a critical temperature where time scales diverge. We see that the MCT fit is valid for almost five orders of magnitude in time even though there is no dynamical arrest at T_c , as the relaxation time of the (2)-TLG diverges only at $\rho = 1$ [10]. A similar MCT power law fit (not shown) can be made for the (1)-TLG, valid for about 2 orders of magnitude.

Fig. 3(b) shows the relaxation time on a reduced temperature scale in the manner proposed by Angell [2]. Here, T_g is defined as the temperature at which $\tau_\alpha = 10^7$. We see that the relaxation time of the (1)-TLG is Arrhe-

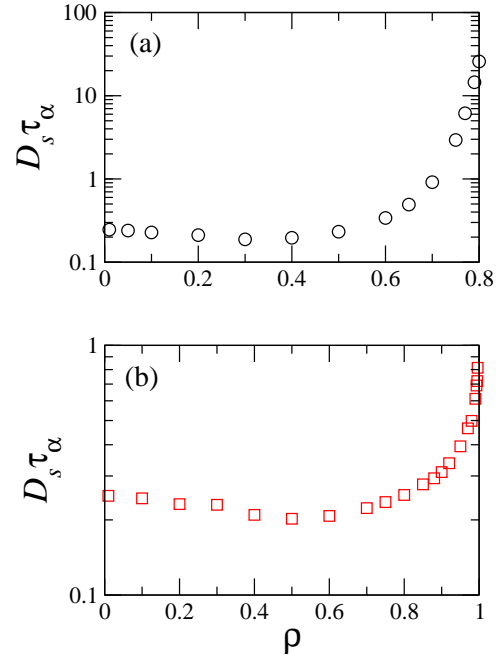


FIG. 6: Stokes-Einstein violation in the (a) (2)-TLG and (b) (1)-TLG.

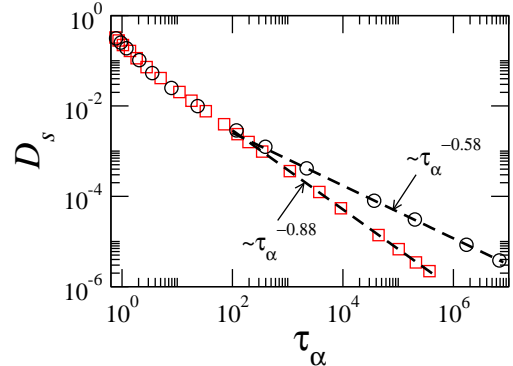


FIG. 7: Fractional Stokes-Einstein exponent: scaling of the self-diffusion constant with relaxation time. The dashed lines are fits to the data at longer times.

nius growing as $\tau_\alpha \sim c^{-\Delta}$ with $\Delta = 2.29$, as $\rho \rightarrow 1$. The relaxation of the (2)-TLG in contrast is super-Arrhenius, and the low temperature data can be fit with a double exponential in $1/T$ [10]. In this context, the (1)-TLG is a strong glassformer whereas the (2)-TLG is a fragile one.

Interestingly, the time exponent $\Delta \approx 2.3$ of the (1)-TLG is the same as that for the one-spin facilitated Fredrickson-Andersen (FA) model in dimension $d = 2$, predicted from renormalization group (RG) calculations and observed numerically [18]. This suggests that the (1)-TLG may be in the universality class of the FA model, the prototypical kinetically constrained spin model for a strong glassformer. We will examine more of these dynamic scaling relations below.

The mean-squared displacement, $\langle |\Delta \mathbf{r}_i(t)|^2 \rangle = \langle |\mathbf{r}_i(t) -$

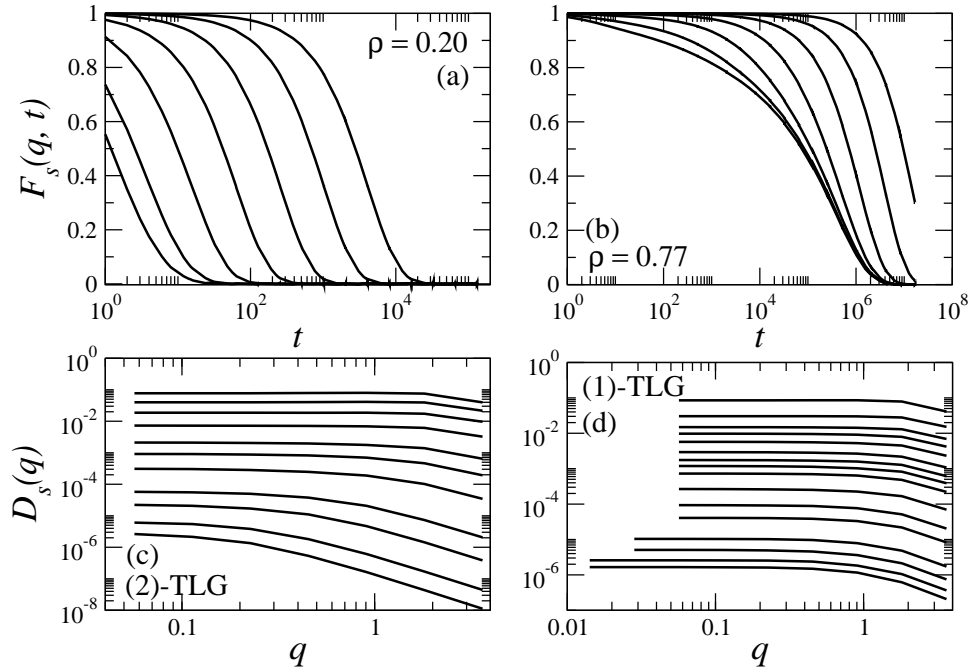


FIG. 8: (Top) Self-intermediate scattering function for the (2)-TLG at various wavevectors: (a) $\rho = 0.20$, (b) $\rho = 0.77$. For both graphs, from left to right: $q = (\pi, 0), (\pi/2, 0), (\pi/4, 0), (\pi/8, 0), (\pi/16, 0), (\pi/32, 0), (\pi/64, 0)$. (Bottom) $D_s(q) \equiv 1/\tau(q)q^2$ as a function of q at various densities: (c) (2)-TLG, (from top to bottom) $\rho = 0.20$ to 0.80 ; (d) (1)-TLG (from top to bottom), $\rho = 0.40$ to 0.996 . The higher density curves for the (1)-TLG include smaller q values because of larger system sizes (see section II).

$\mathbf{r}_i(0)|^2\rangle$, is shown in Fig. 4. The self-diffusion coefficient, D_s , is defined as $D_s = \lim_{t \rightarrow \infty} \langle |\Delta \mathbf{r}_i(t)|^2 \rangle / 6t$. The factor of 6 is due to the fact that each particle on the lattice has six nearest neighbors. We see that at low densities, D_s for the (1)-TLG and (2)-TLG coincide and approach the random-walk value of $1/3$ for diffusion on a two dimensional triangular lattice, as expected. At higher densities, D_s for the (1)-TLG is Arrhenius, and scales as $D_s \sim c^2$ as $\rho \rightarrow 1$, see Fig. 5. This result is in agreement with the analytical prediction of Ref. [10]. Moreover, this is also the scaling of the diffusion constant for a probe molecule coupled to the FA model in any dimension [17], further evidence that the (1)-TLG is in the FA model universality class. On the other hand, D_s for the (2)-TLG is super-Arrhenius (see Fig. 5). The behaviour of D_s is similar, qualitatively, to that of τ_α . The quantitative difference in their scaling with density, however, is significant, and is an indication that relaxation behaviors at short and long lengthscales are not the same. We turn to this issue now in both the (1)-TLG and the (2)-TLG.

V. THE BREAKDOWN OF THE STOKES-EINSTEIN RELATION

An important ramification of broadly distributed heterogeneous dynamics is the breakdown of mean-field dynamical relations such as the much studied Stokes-Einstein (SE) relation. This relation says that diffu-

sion scales inversely with the relaxation time, $D_s \tau_\alpha \sim \text{constant}$. It is a quantitative statement of the expectation that the dynamical behavior of normal liquids should be similar at all but the smallest lengthscales. In supercooled liquids this simple mean-field approximation fails [25, 26], and, given the results of previous sections, we would expect a similar violation of the SE relation in the TLG models. We see from Fig. 6 that the SE relation is indeed violated for both the (2)-TLG and the (1)-TLG, the effect being more pronounced in the fragile case. Moreover, we see that the densities at which the product $D_s \tau_\alpha$ begins deviating from constancy coincide

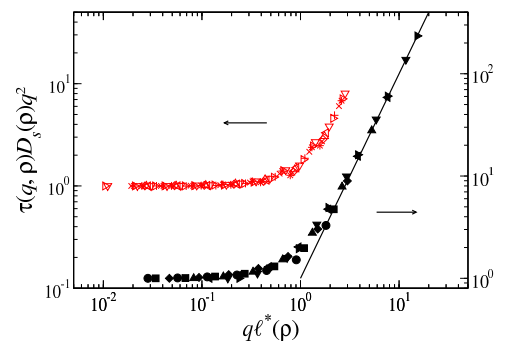


FIG. 9: Data from Fig. 8 collapsed onto a master curve. The filled symbols correspond to the (2)-TLG and the open symbols correspond to the (1)-TLG. The straight line is q^2 .

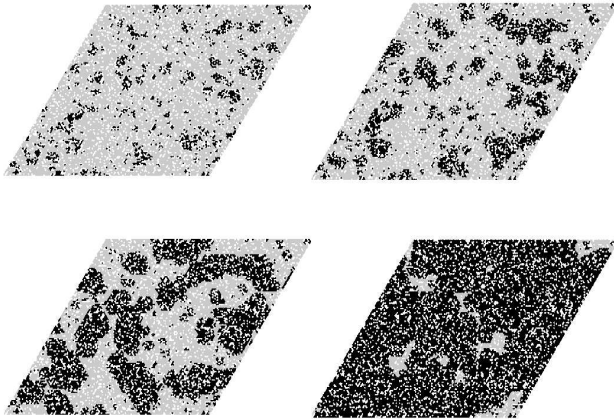


FIG. 10: Growth of mobile particle regions as a function of observation time Δt at $\rho = 0.77$ in the (2)-TLG. Black and grey regions indicate the location of particles and white regions indicate empty lattice sites. Particles colored in black have moved at least one lattice spacing in a time Δt whereas particles colored in gray have not. (Top, from left to right: $\Delta t = 10^3$ and 10^4 ; bottom, from left to right: $\Delta t = 10^5$ and 10^6 ; $\tau_\alpha \sim 10^5$ at this density).

with the onset densities, ρ_o 's, extracted from the distribution of persistence times. This observation reinforces the idea that it is the fluctuation dominated nature of the dynamics that leads to the SE breakdown [17].

SE violation implies that the self-diffusion constant does not scale with the structural relaxation time as τ_α^{-1} . One possibility is that it obeys a fractional SE law, $D_s \sim \tau_\alpha^{-\xi}$ where $\xi < 1$. This is observed in experiments [25], and is obtained theoretically for probe diffusion in the FA and East models [17] (see also [27]). Figure 7 shows that the diffusion constant also obeys a fractional SE law in the TLG models. The SE exponent is $\xi \approx 0.88$ for the (1)-TLG, which is the value expected for the FA model in $d = 2$, $\xi \approx 2/2.3$ [17]. In the case of the (2)-TLG, despite the fact that D_s and τ_α are both super-Arrhenius, we find that the scaling exponent is temperature independent at large densities, $\xi \approx 0.58$. The deviation of this exponent from 1 is larger than that for both the FA and East models in two dimensions [17]. It indicates a larger violation of the SE law, consistent with the fact that the (2)-TLG is more fragile than either of those models [10].

VI. DYNAMICAL LENGTHSCALES

A. Indication of a dynamical lengthscale from a two-point function

Since the growth in timescales and the violation of the Stokes-Einstein relation in the TLG models are clearly not tied to a growth in static lengthscales, we turn now to the

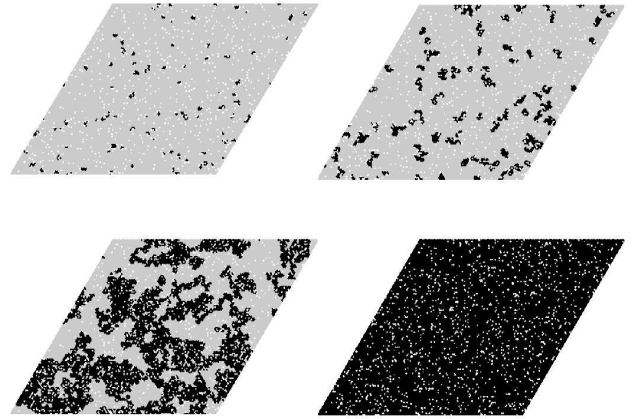


FIG. 11: Same as fig. 10 for the (1)-TLG. Here, $\rho = 0.95$. (Top, from left to right: $\Delta t = 10$ and 10^2 ; bottom, from left to right: $\Delta t = 10^3$ and 10^4 ; $\tau_\alpha \sim 10^3$ at this density).

discussion of dynamical lengthscales. Such a lengthscale can be inferred from examining the relaxation behavior of the self-intermediate scattering function over more than one wavevector at different densities. One can appreciate this fact qualitatively by looking at the decay of $F_s(q, t)$ for the (2)-TLG over several values of q at low and high density, Fig. 8 (top), [19]. At low density, the decay of the various curves looks similar at all wavevectors (except for the largest wavevector) whereas at high density, even the curves at intermediate wavevector differ greatly from the simple exponential form seen at smaller wavevectors. The high density curves bunch up at intermediate to large \mathbf{q} indicating that the relaxation behavior at these lengthscales is different (i.e. slower) than one would expect from the behavior at larger lengthscales. Similar behavior has also been observed in the Kob-Andersen kinetic lattice gas model and kinetically constrained spin models [4, 19].

To quantify the above behavior, we proceed as in [28, 29]. In the hydrodynamic regime, we have $\lim_{q \rightarrow 0} F_s(q, t) \sim \exp(-D_s q^2 t)$, and one expects the product $D_s \tau(q) q^2$ to be independent of \mathbf{q} , where $\tau(q)$ is the time when the intermediate scattering function at wavevector \mathbf{q} decays to $1/e$. In Fig. 8 (bottom), we plot the quantity $D_s(q) \equiv 1/\tau(q)q^2$ as a function of q at various densities. A flat line independent of q indicates normal diffusive behavior whereas a downward bend signifies a change to sub-diffusive behavior. As density increases, the curves begin to bend at a smaller and smaller wavevector, q^* . This behavior is indicative of a growing dynamical lengthscales as density is increased [19, 28, 29].

Following the prescription of [19], we extract a lengthscale, ℓ^* , from Fig. 8 as $\ell^* \sim \sqrt{D_s(q \rightarrow 0) \tau_\alpha}$. This lengthscale determines the onset of Fickian diffusion. Using this lengthscale to rescale space, and using $\tau(q)q^2$ to rescale time, the data from Fig. 8 can be collapsed onto

a master curve, Fig. 9.

B. Direct observation and quantification of a dynamical heterogeneity lengthscale

We can study dynamical lengthscales in the TLG models directly by observing a trajectory over a time Δt and coloring particles which have moved at least one lattice spacing. Snapshots of applying this procedure to trajectories of the (2)-TLG and the (1)-TLG at high particle densities over progressively longer Δt 's are shown in Fig. 10 and Fig. 11. Mobility is indeed correlated: mobile particles are clustered and the clusters of mobility at earlier Δt act as seed particles from which subsequent mobility grows. Moreover, there is a qualitative difference in the shape of the clusters in the (2)-TLG and the (1)-TLG. In the fragile model, the clusters are smooth and more anisotropic, indicating a directed growth of mobile regions. In the strong model, the clusters are rugged and isotropic. These observations can be understood as arising from the difference in the local constraints of both models. The strict two site facilitation rule of the (2)-TLG requires cooperative, hierarchical rearrangement of particles for movement whereas the one site facilitation rule of the (1)-TLG allows for the random diffusion of vacancy pairs [5]. These same correlations between fragility and the smoothness of interfaces and between slow and fast dynamically heterogeneous regions are present in other facilitated models [15, 18, 30].

To quantify the above ideas, we extract a dynamical lengthscale, $\ell(\Delta t)$, from structure factors of the mobile particles [13, 15, 28, 31]. Motivated by the mobility criterion described in the previous paragraph and depicted in Fig. 10 and Fig. 11, we consider the binary field $n_{\mathbf{r}}(t; \Delta t) = p_{\mathbf{r}}(t)[1 - p_{\mathbf{r}}(t + \Delta t)]$, which gives a signal only when there is particle motion at \mathbf{r} over the range of time between t and $t + \Delta t$. Its structure factor is a four point function: it measures a correlation function which depends on two points in time, t and $t + \Delta t$, and two points in space, \mathbf{r} and \mathbf{r}' .

We define the structure factor for the mobility field as the following normalized correlation function:

$$S(\mathbf{q}; \Delta t) = \frac{1}{L^2} \frac{\langle \delta n_{\mathbf{q}}(t; \Delta t) \delta n_{-\mathbf{q}}(t; \Delta t) \rangle}{\langle \delta n_{\mathbf{r}}(t; \Delta t)^2 \rangle} \quad (2)$$

where $\delta n_{\mathbf{r}}(t; \Delta t) = n_{\mathbf{r}}(t; \Delta t) - \langle n_{\mathbf{r}}(t; \Delta t) \rangle$ is the deviation of $n_{\mathbf{r}}$ from its average value and $\delta n_{\mathbf{q}}(t; \Delta t)$ is the Fourier transform of $\delta n_{\mathbf{r}}(t; \Delta t)$:

$$\delta n_{\mathbf{q}}(t; \Delta t) = \sum_{\mathbf{r}} \exp\left(\frac{2\pi i}{L^2} \mathbf{r} \cdot \mathbf{q}\right) \delta n_{\mathbf{r}}(t; \Delta t). \quad (3)$$

The angled brackets, $\langle \dots \rangle$, denote an average over different pairs of configurations along a trajectory separated by a given time interval Δt . We then define the lengthscale, $\ell(\Delta t)$, to be proportional to the inverse of the first

moment, $\bar{q}_{\Delta t}$, of the circularly averaged structure factor, $\tilde{S}(q_n; \Delta t)$ [35]. That is, $\ell(\Delta t) \sim 1/\bar{q}_{\Delta t}$ where:

$$\bar{q}_{\Delta t} = \sum_n q_n \tilde{S}(q_n; \Delta t) / \sum_n \tilde{S}(q_n; \Delta t). \quad (4)$$

Here, $q_n = 2\pi n/L$ and $n = 2, 3, 4, \dots, L/2$. The lengthscale was normalized such that ℓ extracted from the structure factor of a random configuration of particles on the lattice (i.e. an ideal gas) was unity.

Fig. 12(a) and Fig. 12(b) show $\ell(\Delta t)$ at various densities for the (2)-TLG and the (1)-TLG. The basic shape of these curves is as expected: as $\Delta t \rightarrow 0$, mobility is sparse and uncorrelated so ℓ approaches unity and as $\Delta t \rightarrow \infty$, everything becomes mobile and ℓ once again tends towards unity. In between, as the pictures in Fig. 10 and Fig. 11 suggest, mobility clusters together and grows. Looking at the maximum of these different curves, $\ell_{max}(\Delta t_{max})$, a growing lengthscale is clearly evident as ρ increases. It is important to note that, in general, $\ell_{max} \neq \ell^*$ [19]. Fig. 12(c) shows the value of ℓ_{max} plotted versus the structural relaxation time for both the (2)-TLG and the (1)-TLG. At a fixed value of τ_{α} , the dynamical heterogeneity lengthscale for the strong version of the model is larger than that of the fragile version [15]. We also find that the observation time, Δt_{max} , at which the maximum lengthscale, ℓ_{max} , occurs, scales with the structural relaxation time, τ_{α} , for both models.

If the (1)-TLG is in the universality class of the FA model, then we would expect ℓ_{max} to scale as a power of both the excitation concentration, $\ell_{max} \sim c^{-\nu}$, and of the relaxation time, $\ell_{max} \sim \tau_{\alpha}^{1/z}$. This appears to be the case, as shown in Fig. 12(d). For the correlation and dynamic exponents we find $\nu \approx 0.6$ and $1/z \approx 0.25$, in reasonable agreement with the predictions of [18], $\nu = \nu_{\perp} \approx 0.7$ and $1/z = \nu_{\perp}/(1 + \nu_{\parallel}) \approx 0.3$, where ν_{\perp} and ν_{\parallel} are directed percolation exponents [32].

For the (2)-TLG, ℓ_{max} appears to grow logarithmically with τ_{α} , as shown in Fig. 12(c). This would be consistent with free energy barriers growing linearly with the distance between excitations.

VII. DISCUSSION

Despite their simplicity, the constrained lattice gas models we have studied show the essential features of glass forming liquids, such as a precipitous dynamical slowdown and dynamical heterogeneity. They are intermediate between the fully coarse grained kinetically constrained spin models such as the FA and East models, and atomistic models such as the binary Lennard-Jones mixture. From the scaling of the structural relaxation time, τ_{α} , we find that the (2)-TLG is fragile and the (1)-TLG is strong. Fragile behavior versus non-fragile behavior coincides with hierarchical versus diffusive propagation of excitations [5, 33], and the former follows from directional persistence [15]. Dynamic heterogeneity produces length-time scaling and decoupling phenomena. It

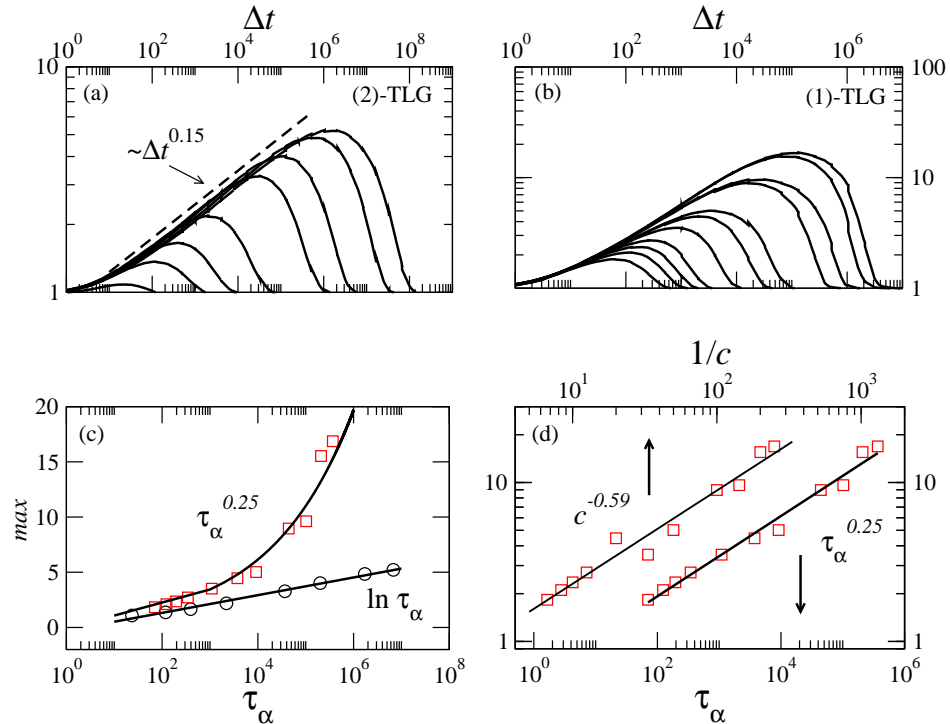


FIG. 12: (Top) Growth of dynamical heterogeneity length as a function of observation time, Δt , for (a) the (2)-TLG, $\rho = 0.50$ to 0.80 ; and (b) the (1)-TLG, $\rho = 0.85$ to 0.996 . (Bottom) Scaling of the maximum value of the dynamical heterogeneity length from (a) and (b) with relaxation time. The growth of ℓ_{max} in the (2)-TLG appears to be logarithmic in time, indicated by the straight line in panel (c), while in the (1)-TLG it follows a power law. Panel (d) shows ℓ_{max} versus τ_α (bottom axis) and c (top axis) for the (1)-TLG, on a log-log scale to highlight power law scaling.

is present in both strong and fragile materials, not only in the latter. This is consistent with recent molecular dynamics simulation on silica [34] and earlier theoretical predictions [15, 16]. Finally, the picture which emerges from comparing the various dynamic scaling exponents to RG predictions is that these models are members of a larger universality classes controlled by dynamical zero temperature critical points [18].

Acknowledgments

This work was supported by the US National Science Foundation, by the US Department of Energy

grant no. DE-FE-FG03-87ER13793, by EPSRC grants no. GR/R83712/01 and GR/S54074/01, and University of Nottingham grant no. FEF 3024. A.C.P. is an NSF graduate research fellow. This research used resources of the National Energy Research Scientific Computing Center, which is supported by the Office of Science of the U.S. Department of Energy under Contract No. DE-AC03-76SF00098.

- [1] M.D. Ediger, C.A. Angell and S.R. Nagel, *J. Phys. Chem.* **100**, 13200 (1996).
- [2] C.A. Angell, *Science* **267**, 1924 (1995).
- [3] P.G. Debenedetti and F.H. Stillinger, *Nature* **410**, 259 (2001).
- [4] W. Kob and H.C. Andersen, *Phys. Rev. E* **48**, 4364 (1993).
- [5] J. Jäckle and A. Krönig, *J. Phys. Condens. Matter* **6**, 7633 (1994); 7655 (1994).
- [6] F. Ritort and P. Sollich, *Adv. Phys.* **52**, 219 (2003).
- [7] D. Kivelson, S.A. Kivelson, X.L. Zhao, Z. Nussinov and G. Tarjus, *Physica A* **219**, 27 (1995).
- [8] X. Xia and P.G. Wolynes, *Proc. Natl. Acad. Sci. USA* **97**, 2990 (2000); J.-P. Bouchaud and G. Biroli, *cond-mat/0406317*.
- [9] J. Kurchan, L. Peliti and M. Sellitto, *Europhys. Lett.* **39**, 365 (1997).
- [10] C. Toninelli, G. Biroli and D.S. Fisher, *Phys. Rev. Lett.* **92**, 185504 (2004); C. Toninelli and G. Biroli, *cond-mat/0402314*.

- [11] E. Marinari and E. Pitard, cond-mat/0404214.
- [12] M.D. Ediger, Annu. Rev. Phys. Chem. **51**, 99 (2000).
- [13] S.C. Glotzer, J. Non-Cryst. Solids, **274**, 342 (2000).
- [14] D.N. Perera and P. Harrowell, J. Chem. Phys. **111**, 5441 (1999).
- [15] J.P. Garrahan and D. Chandler, Phys. Rev. Lett. **89**, 035704 (2002); Proc. Natl. Acad. Sci. USA **100**, 9710 (2003).
- [16] L. Berthier and J.P. Garrahan, J. Chem. Phys. **119**, 4367 (2003); Phys. Rev. E **68**, 041201 (2003).
- [17] Y.J. Jung, J.P. Garrahan and D. Chandler, Phys. Rev. E **69**, 061205 (2004).
- [18] S. Whitelam, L. Berthier and J.P. Garrahan, Phys. Rev. Lett. **92**, 185705 (2004); cond-mat/0408694.
- [19] L. Berthier, D. Chandler and J.P. Garrahan, cond-mat/0409428.
- [20] The wavevector dependent quantity, $F_s(q, t)$, was calculated as a Fourier transform on the square lattice. A correspondence can be made between the reciprocal lattice vectors of the square and triangular lattices as in [5].
- [21] M.E.J. Newman and G.T. Barkema, *Monte Carlo Methods in Statistical Physics* (Oxford University Press, Oxford, 1999).
- [22] R. Yamamoto and A. Onuki, Phys. Rev. E **58**, 3515 (1998).
- [23] D. Richter, B. Frick and B. Farago, Phys. Rev. Lett. **61**, 2465 (1988).
- [24] W. Götze and L. Sjögren, Rep. Prog. Phys. **55**, 55 (1992).
- [25] S.F. Swallen, P.A. Bonvallet, R.J. McMahon and M.D. Ediger, Phys. Rev. Lett. **90**, 015901 (2003).
- [26] I. Chang and H. Sillescu, J. Phys. Chem. B **101**, 8794 (1997).
- [27] K.S. Schweizer and E.J. Saltzman, to appear in J. Phys. Chem. B (2004).
- [28] L. Berthier, Phys. Rev. E **69**, 020201(R) (2004).
- [29] M.D. Ediger et al., unpublished.
- [30] L. Berthier and J.P. Garrahan, cond-mat/0410076.
- [31] N. Lacevic, F.W. Starr, T.B. Schröder and S.C. Glotzer, J. Chem. Phys. **119**, 7372 (2003).
- [32] H. Hinrichsen, Adv. Phys. **49**, 815 (2000).
- [33] R. G. Palmer, D. L. Stein, E. Abraham, and P. W. Anderson, Phys. Rev. Lett. **53**, 958 (1984).
- [34] M. Vogel and S.C. Glotzer, Phys. Rev. Lett. **92**, 255901 (2004).
- [35] J.G. Amar, F.E. Sullivan, and R.D. Mountain, Phys. Rev. B **27**, 196 (1988).